OPEN ACCESS



ALMA 1.1 mm Observations of a Conservative Sample of High-redshift Massive Quiescent Galaxies in SHELA

Katherine Chworowsky¹ , Steven L. Finkelstein¹ , Justin S. Spilker²,³ , Gene C. K. Leung¹ , Micaela B. Bagley¹ , Caitlin M. Casey¹ , Caryl Gronwall⁴,⁵ , Shardha Jogee¹ , Rebecca L. Larson¹ , Casey Papovich²,³ , Rachel S. Somerville⁵ , Matthew Stevans¹ , Isak G. B. Wold²,8,9 , and L. Y. Aaron Yung¹

1 Department of Astronomy, The University of Texas at Austin, Austin, TX 77812, USA
2 Department of Physics and Astronomy, Texas A&M University, College Station, TX 77843-4242, USA
3 George P. and Cynthia Woods Mitchell Institute for Fundamental Physics and Astronomy, Texas A&M University, College Station, TX 77843-4242, USA
4 Department of Astronomy & Astrophysics, The Pennsylvania State University, University Park, PA 16802, USA
5 Institute for Gravitation and the Cosmos, The Pennsylvania State University, University Park, PA 16802, USA
6 Center for Computational Astrophysics, Flatiron Institute, 162 5th Avenue, New York, NY 10010, USA
7 Astrophysics Science Division, Goddard Space Flight Center, Greenbelt, MD 20771, USA
8 Department of Physics, The Catholic University of America, Washington, DC 20064, USA
9 Center for Research and Exploration in Space Science and Technology, NASA/GSFC, Greenbelt, MD 20771, USA
10 Astrophysics Science Division, NASA Goddard Space Flight Center, 8800 Greenbelt Rd, Greenbelt, MD 20771, USA
8 Received 2022 November 14; revised 2023 April 21; accepted 2023 May 1; published 2023 July 3

Abstract

We present a sample of 30 massive ($\log(M_*/M_\odot) > 11$) z = 3-5 quiescent galaxies selected from the Spitzer-HETDEX Exploratory Large Area (SHELA) Survey and observed at 1.1 mm with Atacama Large Millimeter/submillimeter Array (ALMA) Band 6 observations. These ALMA observations would detect even modest levels of dust-obscured star formation, on the order of $\sim 20\,M_\odot$ yr⁻¹ at $z \sim 4$ at the 1σ level, allowing us to quantify the amount of contamination from dusty star-forming sources in our quiescent sample. Starting with a parent sample of candidate massive quiescent galaxies from the Stevans et al. v1 SHELA catalog, we use the Bayesian BAGPIPES spectral energy distribution fitting code to derive robust stellar masses (M_*) and star formation rates (SFRs) for these sources, and select a conservative sample of 36 candidate massive ($M_* > 10^{11}\,M_\odot$) quiescent galaxies, with specific SFRs $> 2\sigma$ below the Salmon et al. star-forming main sequence at $z \sim 4$. Based on the ALMA imaging, six of these candidate quiescent galaxies show the presence of significant dust-obscured star formation, and thus were removed from our final sample. This implies a $\sim 17\%$ contamination rate from dusty star-forming galaxies with our selection criteria using the v1 SHELA catalog. This conservatively selected quiescent galaxy sample at z = 3-5 will provide excellent targets for future observations to constrain better how massive galaxies can both grow and shut down their star formation in a relatively short period.

Unified Astronomy Thesaurus concepts: Galaxy evolution (594); Submillimeter astronomy (1647); Quenched galaxies (2016); Galaxies (573)

1. Introduction

Traditionally, it is well established observationally that galaxies follow a strong bimodal color and morphological distribution. Galaxies that are disk dominated and star forming show strong blue colors, whereas spheroid dominated galaxies that have stopped forming stars and have predominantly old stellar populations are generally red (Baldry et al. 2004; Balogh et al. 2004; Bell et al. 2004). While recent results have pointed to a more nuanced understanding of galaxy colors and populations, and exceptions exist within this bimodality (Newman et al. 2018; Fraser-McKelvie & Cortese 2022), the majority of galaxy populations still fall within this dichotomy, providing us with a powerful tool for characterizing galaxies. The most-massive galaxies in the local universe are also quiescent, forming stars well below the stellar mass and star formation relation. The stellar mass and number densities of these galaxies has increased significantly since $z \sim 2$, while the mass density of star-forming galaxies has stayed roughly constant (e.g., Kriek et al. 2006; Faber et al. 2007; Brammer et al. 2011; Fang et al. 2012;

Original content from this work may be used under the terms of the Creative Commons Attribution 4.0 licence. Any further distribution of this work must maintain attribution to the author(s) and the title of the work, journal citation and DOI.

Muzzin et al. 2013; Brennan et al. 2015). This implies that there is some physical mechanism causing star formation activities to cease, commonly referred to as the process of "quenching."

To attempt to understand the dominant mechanisms responsible for quenching, one can turn to simulations of galaxy formation. Modern theoretical models are able to reproduce the present day observed quiescent population through a combination of physical effects (e.g., active galactic nuclei, AGNs, activity, disk instabilities, and mergers). There is now a general consensus that the dominant mechanism leading to the continuation of quenching, suppressing star formation not only on short timescales but producing galaxies that remain passive through time, is related to feedback from AGNs (AGN feedback; e.g., Springel et al. 2005; Fabian 2012; Choi et al. 2014; King & Pounds 2015; Somerville & Davé 2015, and references within). Historically it has been a challenge for modern theoretical models and simulations to reproduce the observed population of massive quiescent galaxies at higher redshift (z > 4), with most models and simulations severely underpredicting the number densities of quiescent sources compared to observations (Brennan et al. 2015; Merlin et al. 2018; Cecchi et al. 2019; Merlin et al. 2019; Valentino et al. 2020). Constraining when these galaxies appear in the universe and their abundance at high redshift can provide critical

constraints on the physics responsible for forming and evolving massive galaxies in the early universe.

Many studies have measured the number densities of quiescent galaxies or the quiescent fraction out to high redshift using selection criteria based on broadband colors and physical properties derived from photometric spectral energy distribution (SED) fitting (e.g., Muzzin et al. 2013; Spitler et al. 2014; Brennan et al. 2015; Stefanon et al. 2015; Glazebrook et al. 2017; Merlin et al. 2018; Schreiber et al. 2018; Davé et al. 2019; Merlin et al. 2019; Forrest et al. 2020; Valentino et al. 2020; Dickey et al. 2021), while recent studies with JWST find a significant population of massive quiescent galaxies at z = 3-5 (Carnall et al. 2022), implying that star formation occurs on faster timescales and quenching more efficiently than predicted by most models. However, in order to understand fully the timescale of formation for these galaxies, we not only need to identify these galaxies, we must also gather a consensus of their number densities across redshift. Currently, number densities for massive quiescent galaxy samples at high redshift often differ from one study to another, largely due to differing definitions of quiescence as well as the fact that these surveys have typically probed relatively small volumes contributing to large statistical uncertainties and high field-to-field variance.

Stevans et al. (2021) attempted to overcome this statistical uncertainty by performing the current largest volume systematic search for massive quiescent galaxies in the early universe using deep multiwavelength imaging across a wide area within the Spitzer-HETDEX Exploratory Large Area (SHELA) field (Papovich et al. 2016). Stevans et al. (2021) presented a photometric catalog, along with a catalog of galaxy properties from SED fitting for massive galaxies $(M_*/M_{\odot} > 10^{11})$ at z = 3-5. Due to the red nature these galaxies in the optical infrared (IR) range, often times optical-IR-selected samples of high-redshift massive quiescent galaxies are contaminated by lower-redshift dust-obscured star-forming galaxies. Thus, while Stevans et al. (2021) initially selected a sample of \sim 500 quiescent candidate galaxies, in order to limit contamination, they only published an extremely conservative sample of nine candidate massive quiescent galaxies which satisfied all of their cuts even when including a redshift-luminosity prior. This represents a lower limit on the number density in the SHELA field. For this study we seek to improve upon selection by investigating potential contaminants in the Stevans et al. (2021) parent sample, prior to the application of a redshift-luminosity prior.

The somewhat limited depth of ground-based optical observations mean that many candidate quiescent galaxies have SEDs which are also consistent with dusty star-forming galaxies (DSFGs). The presence of dust suppresses emission at UV and optical ranges, while heating of this dust by massive stars results in increased flux at far-IR (FIR) or submillimeter wavelengths, allowing us to distinguish easily between starforming and quiescent galaxies that may look similar in the optical-IR range. The deployment of the Atacama Large Millimeter/submillimeter Array (ALMA) allows constraints on the dust emission of the massive galaxy population (e.g., Capak et al. 2015; Maiolino et al. 2015; Scoville et al. 2016; Schreiber et al. 2017; Casey et al. 2018). By looking at candidate massive quiescent galaxies with ALMA, we can confidently constrain the presence of obscured star formation across large redshift ranges, thus ruling out dusty star-forming sources in samples (Schreiber et al. 2018; Santini et al. 2019).

In this paper we present the results from ALMA follow up of 100 of the original sample of quiescent candidates from Stevans et al. (2021). We improve upon their selection by deriving galaxy properties from a conservative and more robust SED-fitting reanalysis of these 100 candidates. Using both eazy and BAGPIPES, we constrain the photometric redshift and physical parameters of each galaxy, further honing those which are likely to be truly quiescent. We present ALMA Cycle 7 Band 6 1.1 mm observations for these sources to probe for obscured star formation, ultimately arriving at a higherconfidence and more-complete sample of massive quiescent galaxies. This paper is organized as follows: in Section 2 we present our parent sample from SHELA. Our method of determining photometric redshifts with eazy and deriving galaxy properties with BAGPIPES is described in Section 3. Our ALMA data and measurements are detailed in Section 4. We discuss the expected contamination of our selection process based on the ALMA results in Sections 5 and 6, and we summarize our work and discuss future work in Section 7. Where applicable, we assume a cosmology of $H_0 = 70 \text{ km s}^{-1}$ Mpc⁻¹, $\Omega_M = 0.3$, and $\Omega_{\Lambda} = 0.7$. All magnitudes given are in the AB system (Oke & Gunn 1983).

2. Data

We select our sample of massive quiescent galaxies from the SHELA survey. The SHELA data set includes modest-depth (22.6 AB mag, 50% completeness) 3.6 μ m and 4.5 μ m imaging from Spitzer/IRAC (Papovich et al. 2016), u'g'r'i'z' imaging from the Dark Energy Camera over 18 deg² (DECam; Wold et al. 2019), VISTA J and K_s photometry from the VICS82 survey (Geach et al. 2017), and a growing database of full-field IFU spectroscopy from the Hobby-Eberly Telescope Dark Energy Survey (HETDEX; Hill et al. 2008; Gebhardt et al. 2021), where the HETDEX observations in SHELA are presently $\sim 20\%$ complete. Stevans et al. (2021) also obtained imaging with NEWFIRM on the KPNO Mayall 4 m telescope with the NEWFIRM HETDEX Survey (NHS; PI: Finkelstein), a moderately deep K_s (2.1 μ m) near-IR imaging survey, adding deeper $K_s = 22.4$ mag (5 σ) imaging across 22 deg². These K_s -band data reduce the fraction of catastrophic errors in photometric redshifts and measure robust star formation rates (SFRs) by breaking the age-dust degeneracy. The SHELA field has also been observed by Herschel/SPIRE at 0.25-0.5 mm (PI: Viero; Viero et al. 2014), however, these data are very shallow, sensitive to obscured SFRs $> 200 \, M_{\odot} \, {\rm yr}^{-1}$ at $z \sim 1$, and $> 1000 \, M_{\odot} \, {\rm yr}^{-1}$ at $z \sim 3$, much higher than the expected SFRs of the contaminants we search for here; therefore, these data were not included in the analysis presented.

2.1. Initial Sample

Stevans et al. (2021) constructed a multiwavelength (0.4–4.5 μ m) K-band-selected catalog, using Tractor (Lang et al. 2016) to deblend the IRAC photometry. To perform their selection of massive galaxies at z>3, Stevans et al. (2021) required a 5σ or greater detection significance in K_s , a 2σ or greater detection in IRAC 3.6 μ m, and a u'-band signal-tonoise ratio (S/N) < 2, as well as a measurement in all optical DECam bands to allow for reliable constraints on $z_{\rm phot}$. Stevans et al. (2021) then used eazy-py¹¹, based on the eazy code

¹¹ Version 0.2.0-16-g6ab4498; https://github.com/gbrammer/eazy-py.

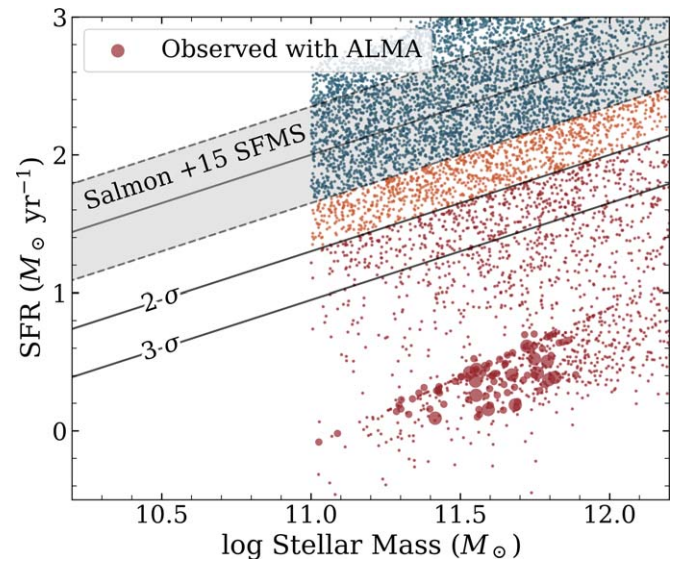


Figure 1. The small data points show the z=3-5 massive $(\log (M_*/M_\odot) > 11)$ sample from Stevans et al. (2021). The blue, orange, and red circles denote star-forming, moderately star-forming, and quiescent galaxies, respectively. The red circles are sources with ALMA observations presented here, shown with the Stevans et al. (2021) eazy-py-based SFR and stellar mass values. The larger red circles are $>3\sigma$ detections with ALMA. We also show the Salmon et al. (2015) z=4 SFMS, with lines highlighting the regions of 1σ , 2σ , and 3σ scatter from the main trend.

(Brammer et al. 2008), to measure photometric redshifts and stellar population properties for all 1.53 million cataloged galaxies in SHELA. To fit galaxy SEDs, eazy-py finds the linear combination of 12 Flexible Stellar Population Synthesis (FSPS) templates (Conroy et al. 2009; Conroy & Gunn 2010) that minimizes χ^2 with respect to the fluxes in all available photometric bands. For this initial sample, Stevans et al. (2021) ran eazy-py with flat priors and selected a parent sample of 3684 massive galaxies ($\log(M_*/M_\odot) > 11$) which have significant detection in K and both IRAC bands with >60% of their integrated photometric redshift probability density (P(z)) at 3 < z < 5. Of these galaxies, Stevans et al. (2021) found 506 likely quiescent sources, with $\log(sSFR/yr^{-1}) < -11$.

Stevans et al. (2021) also explored the possibility of contamination by red galaxies at low redshift, which can have SED shapes that appear similar to z=3-5 quiescent galaxies within our filter set. They attempted to minimize contamination by using an apparent magnitude prior, which applies a Bayesian prior based on a source's apparent magnitude. eazy has a built-in prior, derived based on the luminosity functions of the De Lucia & Blaizot (2007) semianalytic model (SAM), which resulted in only nine of the original 506 quiescent candidates being classified as massive quiescent galaxies. Stevans et al. (2021) noted that this likely results in significant incompleteness in the published sample.

In this study, we chose to revisit their initial parent sample to investigate the contamination by low-redshift dusty sources. To achieve this, ALMA Cycle 7 Band 6 1.1 mm observations (rms = 80 μ Jy) were obtained for a selected subsample of 100/506 massive quiescent candidates (PI: Finkelstein). The target sample is selected to span 3 < z < 5, $\log(M/M_{\odot}) = 11.1-11.9$, $20 < K_s < 22$, with $\log(\text{sSFR/yr}^{-1}) < -11$ (Figure 1). We perform the subsequent analysis on this subset of 100 candidate massive quiescent candidates.

3. Selecting Massive Quiescent Galaxies

3.1. Photometric Redshifts with eazy

While Stevans et al. (2021) performed SED fitting using the python version of eazy, eazy-py, we elected to perform an independent photometric redshift selection using the more well-tested command-line version of eazy, using the same set of twelve FSPS (Conroy et al. 2009; Conroy & Gunn 2010) templates ("tweak_fsps_QSF_12_v3") as Stevans et al. (2021), which utilize a Chabrier (2003) initial mass function, Kriek & Conroy (2013) dust law, and solar metallicity. These FSPS models span a wide range of galaxy types (star forming, quiescent, and dusty), with different realistic star formation histories (SFHs; bursty and slowly rising). The best-fit combination of templates is determined through χ^2 minimization.

As described above, Stevans et al. (2021) elected to include a redshift–luminosity prior in their selection of quiescent galaxies. eazy has such a built-in prior, based on the De Lucia & Blaizot (2007) SAM. These priors are typically peaked at low redshift with a tail to higher redshift, with the tail becoming more prominent at fainter magnitudes. This prior will typically make any low-redshift solution be the dominant solution, even if the higher-redshift solution is a better fit to the photometry. However, the accuracy of luminosity function of galaxies in the De Lucia & Blaizot (2007) SAM is in doubt, as the red $(B-V \geqslant 0.5)$ galaxy density at $z \sim 3$ in this SAM underpredicts the observed density by a factor of \sim 8 (Marchesini & van Dokkum 2007). Therefore, we elect to perform our SED fitting without a redshift–luminosity prior to mitigate the possible effects of an unreliable prior.

To select our candidate high-redshift sources, we require the integral of the normalized redshift probability distribution function (PDF) to be >70% for z>2.5, compared to Stevans et al. (2021)'s cut of >60% for z>3. Of our initial sample of 100 candidate quiescent galaxies observed with ALMA, 61 satisfied this photometric redshift cut, forming our high-redshift sample.

3.2. SED Fitting with BAGPIPES

While eazy provides a robust photometric redshift determination, due to the small set of templates, it has a limited ability to explore the full parameter space of the physical properties of galaxies. Thus, in order to determine the stellar masses and SFRs of our sources, we utilize the BAGPIPES modeling code. BAGPIPES is a Bayesian spectral fitting code which models the emission from galaxies from the far-UV to the millimeter regime, allowing the user to build up complex models for fitting, with user-defined stellar population synthesis models, SFHs, and dust attenuation and emission models. BAGPIPES is a Python tool, and can fit these models to arbitrary combinations of spectroscopic and photometric data using the MULTINEST nested sampling algorithm (Carnall et al. 2018).

After using eazy to generate our sample of high-redshift sources, we run BAGPIPES on the SHELA observations. We modify BAGPIPES to take as input the redshift probability distribution as determined by eazy as a prior on the modeled redshift. We further force BAGPIPES to ignore any potential low-redshift solution (already limited to <30% of the redshift probability density) by setting P(z < 2.5) to zero. This allows us to assume that the high-redshift solution is generally correct,

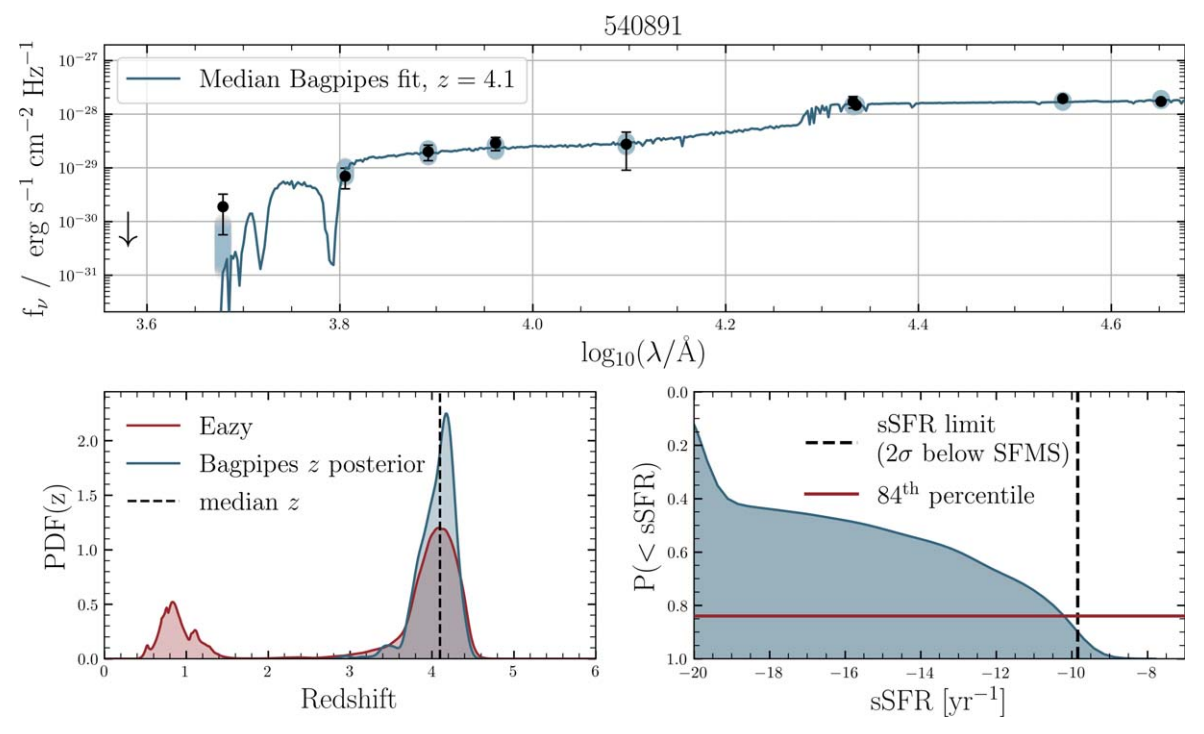


Figure 2. An example of BAGPIPES results for a single source. The median SED is plotted in the top panel. The black points show the observed fluxes from SHELA and the blue shaded points are the 1σ range of the posterior photometry. The lower left plot shows the redshift distribution from eazy in red, and the posterior redshift distribution from BAGPIPES in blue. The bottom right panel shows the posterior on the sSFR: the black dashed line shows the sSFR limit for our quiescent selection, and the red line shows the median value of the posterior on sSFR.

Table 1
Fixed and Fitted Parameters with Their Associated Priors for the Declining Exponential SFH Model and Salim et al. Dust Models, Assuming a Kroupa Initial Mass Function

Parameter	Prior	limits	
age/Gyr	Uniform	(0.1, 15)	
$\log_{10}(M_{\mathrm{form}}/M_{\odot})$	Uniform	(1, 15)	
$\log_{10}(U)$	Uniform	(-4, 2)	
Z/Z_{\odot}	Uniform	(0, 2.5)	
$ au/\mathrm{Gyr}$, timescale of decrease in the SFH	Logarithmic	(0.3, 10)	
A_V	Uniform	(0, 8)	
δ , deviation from the Calzetti slope	$Gaussian_{\mu=0,\sigma=0.1}$	(-0.3, 0.3)	
B, 2175 Å bump strength	Uniform	(0, 5)	
Zobs	eazy $P(z)$	Variable	

Note. M_{form} is the total mass of stars formed by the galaxy up to time τ , δ and B are parameters unique to the Salim et al. (2018) dust models. Priors listed as logarithmic are uniform in log space.

essentially implementing an additional prior that each source is at z>2, but also to generate a posterior probability distribution of the stellar mass and SFR of each source with uncertainties inclusive of the photometric redshift uncertainties. We elected to include the photometric redshift prior since eazy is optimized for photometric redshift recovery, whereas BAG-PIPES is allowed to explore a large range of parameter space. Furthermore, allowing for lower-redshift solutions would result in unphysical marginalized uncertainties on the physical parameters of interest, which would combine both low- and high-redshift solutions. Therefore, by constraining the redshift space, we force BAGPIPES to explore a wider range of galaxy parameters within the likely redshift of each source.

As our parent sample was initially selected to be quiescent, each galaxy was fit with a declining exponential SFH with a logarithmic prior on τ , the timescale of star formation decline; the complete fit parameters are listed in Table 1. We also compared BAGPIPES' ability to probe the complete parameter space by changing the number of live points (n_live) in the Markov Chain Monte Carlo fit and found that a value of 3000 live points produces the best-fit results within a reasonable fit time. Each SED fit is returned with a posterior distribution in mass and SFR (an example is shown in Figure 2), from which we classify sources as quiescent based on the distribution of the specific SFR (sSFR) posterior. SEDs for the entire high-redshift sample can be seen in Figures 10 and 11 in the Appendix.

To determine which of our sources are likely quiescent, we compare the derived sSFRs to the z = 4 star-forming main sequence (SFMS) as presented in Salmon et al. (2015). To be classified as quiescent, we require 84% of the sSFR posterior to be $>2\sigma$ below the SFMS at the best-fit photometric redshift. We note that this is a much more conservative selection than the typical process of using best-fit values. In fact, while the majority of our galaxies have an sSFR median well below the SFMS at the best-fit stellar mass, this method allows us to encompass the full uncertainty on the sSFR posterior due to other possible solutions in our SED modeling. We also note the difference from the Stevans et al. (2021) selection, who used a fixed sSFR threshold of $\log(sSFR/yr^{-1}) < -11$. By using the z = 4 main sequence as a threshold, our selection accounts for the evolution of typical galaxy sSFRs to higher values with increasing redshift (Speagle et al. 2014; Rinaldi et al. 2022; Sandles et al. 2022). With this conservative selection, we find that 36 out of the 61 high-redshift sources were classified as

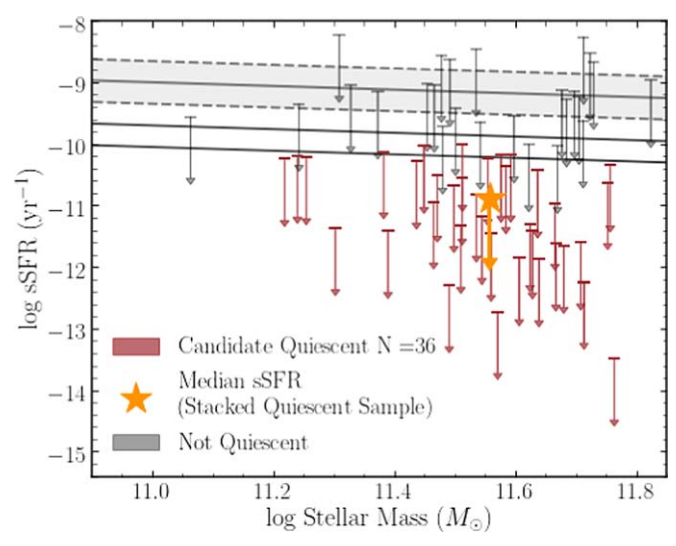


Figure 3. The sSFR vs. stellar mass distribution of our 61 high-redshift sources. The gray shaded region is the 1σ range of the Salmon et al. (2015) SFMS, the gray solid lines are 2σ and 3σ below the SFMS. To be classified as quiescent, we require 84% of the integral of the P(sSFR) from BAGPIPES to fall below 2σ of the SFMS for the given best-fit stellar mass (red). For the sources not selected as quiescent (gray arrows), the majority have an sSFR median well below the SFMS at the best-fit stellar mass. However, their sSFR distributions are broad, such that the 84% of the integral of the P(sSFR) falls above our 2σ selection. For the 36 quiescent candidates shown in red, we plot the upper limits from our BAGPIPES fit if the median of the SFR is less than $0.1~M_{\odot}~\text{yr}^{-1}$, which is the case for all sources. The yellow star shows the median stellar mass and sSFR measured from SHELA for the sample of 36 candidate massive quiescent galaxies.

quiescent based on optical–IR SED fitting. These sources are shown in Figure 3. To summarize, based on our updated photometric redshifts and stellar population modeling, we consider 36 of the original 100 ALMA-observed galaxies from Stevans et al. (2021) to be robust candidate massive quiescent z > 3 galaxies, with the smaller number due to our more-advanced selection procedure.

4. ALMA Observations

For the sample of galaxies presented here, we have obtained ALMA Band 6 1.1 mm observations in Cycle 7 program 2019.1.01219.S (PI: Finkelstein). These data were obtained in 2019 December. Each source was observed 6×26.4 s, for a total integration time of 158 s for each source. While relatively short integrations, the sensitivity of ALMA allows us to reach sufficiently deep to detect dust emission from contaminating DSFGs robustly (and possibly detect weak low-level star formation from truly quiescent galaxies). Figure 4 illustrates how the SEDs of quiescent and DSFGs diverge at longer wavelengths, where rest-frame FIR observations to a sensitivity of 80 μ Jy at 1.1 mm made with ALMA can robustly rule out star-forming solutions for our quiescent candidates.

We use the default continuum images of each source produced by the ALMA pipeline in our analysis. These images use Briggs weighting with robustness parameter 0.5, and reach a typical spatial resolution of 1.730×0.780 (corresponding to a physical size of order 9×6 kpc at z = 4). For quiescent sources, we do not expect these galaxies to be spatially resolved in our ALMA observations, as high-redshift quiescent galaxies are often compact, with half-light sizes of a few kiloparsecs (Stefanon et al. 2013; Straatman et al. 2015). For

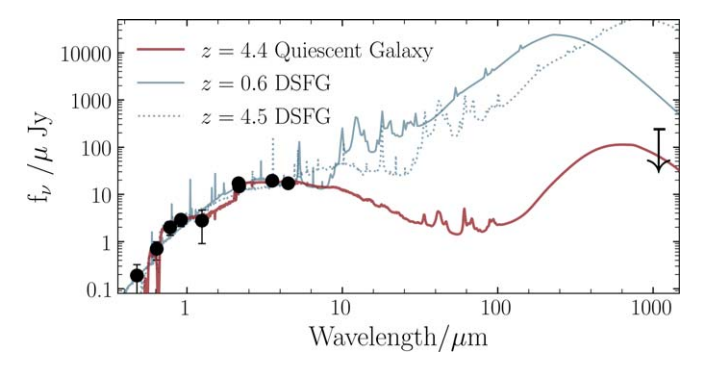


Figure 4. Example photometry of one of our quiescent sources (black) with the best-fit BAGPIPES SED and example DSFG SEDs at both low and high redshifts. Although the SHELA photometry is best fit to a high-redshift quiescent galaxy (red) with sSFR = -10.3, it is also consistent with a high-redshift DSFG with sSFR = -8.0 (dotted blue) and a low-redshift DSFG solution with sSFR = -8.5 (solid blue). The ALMA 3σ depth is shown in the downward arrow, significantly ruling out dust-obscured star formation at any redshift.

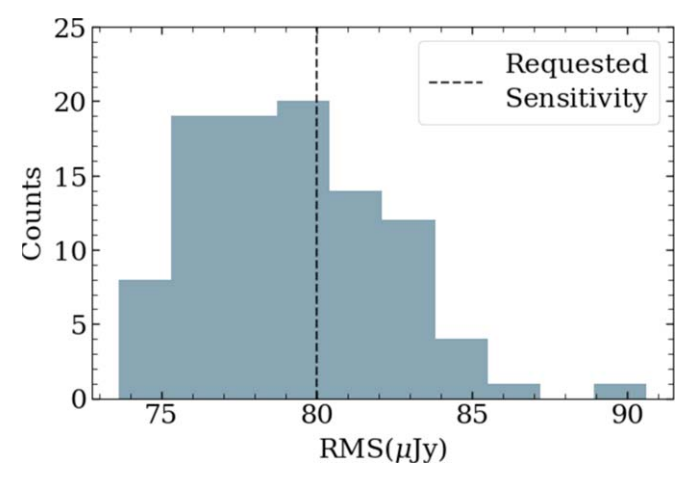


Figure 5. The distribution of the rms in our 98 ALMA observations. The reported rms values are calculated by removing pixels with $>5\sigma$ detections, and then calculating the rms of the remaining pixels. The median rms is 79 μ Jy, with a standard deviation of 3 μ Jy, comparable to our desired sensitivity of 80 μ Jy.

sources with possible IR emission (i.e., dust-obscured star-forming galaxies), previous studies using sufficient ALMA resolution measured sizes which suggest that dust emission takes place within compact regions of the galaxy, with observed $R_e(\text{FIR})$ to be generally smaller than $R_e(\text{optical})$, on order of $\lesssim 2$ kpc at $z \sim 3$, (Fujimoto et al. 2017; Ikarashi et al. 2017; Franco et al. 2018). In both cases, quiescent or DSFGs, the galaxy is expected to be roughly point-like for the spatial resolution of the presented observations.

From the 100 targets observed, we visually examined each source's observations and removed two due to observational artifacts, resulting in 98 sources with reliable data. We measured the sensitivity in each observation as the 5σ clipped rms of the images from the non–primary-beam corrected map. We show the distribution from our 98 observations in Figure 5. The median value of all images is $79 \pm 3~\mu \mathrm{Jy}~\mathrm{beam}^{-1}$. Of the 36 robust candidate high-redshift massive quiescent galaxies, all had reliable data, and we perform the following analysis on this subsample. We also present results from the 62 sources not included in our subsample in Appendix B.

Table 2

ALMA Fluxes and Obscured SFRs of the Six Sources from Our Initial Sample of 36 Candidate Quiescent Galaxies Removed Based on Flux Measurements in ALMA 1.1 mm Imaging, Assuming These Sources Are at the eazy Photometrically Fitted Redshifts

SHELA ID	z_a	K-band Mag	ALMA 1.1 mm flux (μJy)	Obscured SFR $(M_{\odot} \text{ yr}^{-1})$	sSFR (yr ⁻¹)
406680	3.2	21.2	251 ± 79	66 ± 25	-9.8 ± 0.2
130774	3.2	21.1	254 ± 80	60 ± 21	-9.7 ± 0.1
309122	3.1	20.0	236 ± 76	56 ± 20	-10.0 ± 0.2
928088	3.1	20.8	249 ± 82	62 ± 22	-9.7 ± 0.2
399980	4.2	20.8	204 ± 77	46 ± 16	-9.8 ± 0.1
444706	4.5	21.3	225 ± 80	50 ± 18	-9.7 ± 0.2

Note. These galaxies were classified as quiescent based on SED fitting of SHELA photometry. However, their fluxes at ALMA 1.1 mm indicate the presence of obscured star formation; therefore they were removed from the final sample of quiescent sources. We report the estimated dust-obscured SFRs calculated from a dust model with characteristic dust temperature $T = 45 \pm 5$ K expected from DSFGs at $z \sim 4$. Based on these results, we expect a contamination rate of $\sim 17\%$ in future quiescent samples within SHELA. We report the obscured SFR as described in Section 5.

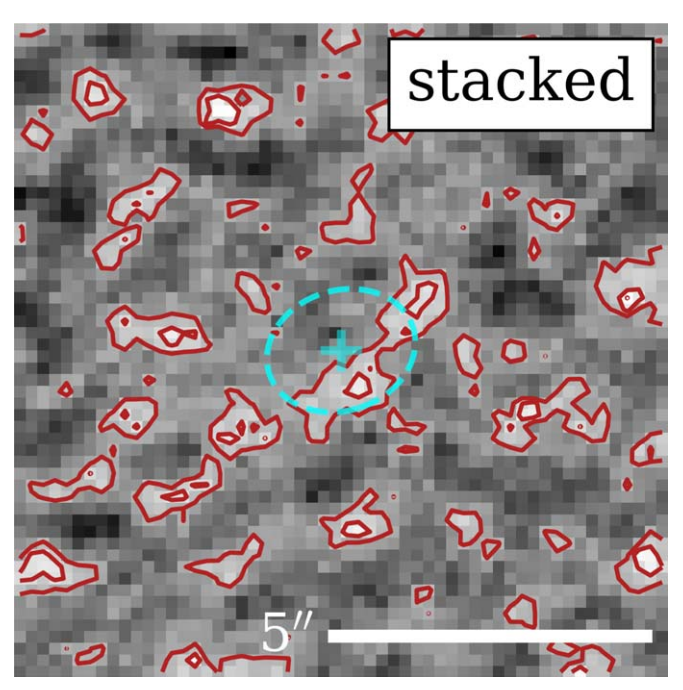


Figure 6. The median stack of our final sample of 30 massive quiescent galaxies. The cyan ellipse is the median ALMA beam centered on the expected source position. The red denotes 1σ and 2σ contours, and the measured flux is $9~\mu Jy \pm 17~\mu Jy$.

4.1. Astrometric Corrections

To determine the source emission, we first match the source locations between the SHELA and the ALMA observations. The DECam exposures in SHELA were observed through a seven-year period, and the images were reduced using different versions of the NOAO DECam Community Pipeline; therefore, we performed a recalibration of the astrometry and flux scaling of each image uniformly prior to stacking. The process is summarized here, but details can be found in the updated SHELA catalog paper (Leung et al. 2023). The astrometry of each image is tied to the Gaia EDR3 catalog (Marrese et al. 2018). For each image, an initial source catalog is generated using SEP (Barbary 2016) and matched to the reported coordinates of astrometry stars in the Gaia EDR3 catalog. The median *x*-offset and *y*-offset required to match the good stars to the Gaia coordinates in each image was determined and

applied to SHELA to correct the astrometry. We use these astrometric corrected coordinates as the source position in our measurements on the ALMA Band 6 imaging.

4.2. Source Flux Determination

In order to determine the integrated flux of each ALMAobserved source, we employed the Common Astronomy Software Applications (CASA) package's imfit¹² task, which attempts to fit one or more elliptical Gaussian components to an image region. We performed two iterations of imfit. For the first iteration, we fix the elliptical Gaussian to the ALMA synthesized beam shape with the center of the beam allowed to move freely (beam-fixed). This method allows us to recover accurate fluxes accounting for slight deviations of the source position due to astrometry in the SHELA catalog. In the second iteration, we fix both the elliptical Gaussian to the ALMA synthesized beam shape, and the center to the R.A. and decl. of the source (beam+position-fixed), accounting for nondetections. The initial estimates provided to imfit are chosen to be the astrometrically corrected center of the quiescent candidate and the flux of the pixel at that location, since the sources of interest are unresolved by ALMA.

We use the integrated flux as determined from the beamfixed fit as our fiducial flux value if the fit returns a source with an S/N > 3. Our tests show that at that significance level, imfit is able to find the source center accurately. Four sources (out of the full selected parent sample of 36) were found to have a source with an S/N > 3, and thus were fit in this way. Within these images, we then determine the separation of the imfit determined source from the expected source R.A. and decl. We determine that if the fitted center is within the K-band point-spread function (PSF) with FWHM \sim 1."41, that the emission is indeed coming from the quiescent candidate. All four images with S/N > 3 were determined to be consistent with the quiescent candidates from the parent sample. For the sources for which the beam-fixed fit found an S/N < 3, we chose to use the integrated flux as calculated from the beam+position-fixed fit as the flux of our source, since the reliability of the fitted position for a source with such a low S/N is questionable. The remaining 32 candidate massive quiescent galaxies were all found to have an S/N < 3at the center, therefore we chose to report the flux calculated from the beam+position-fixed fits.

¹² https://casa.nrao.edu/docs/taskref/imfit-task.html

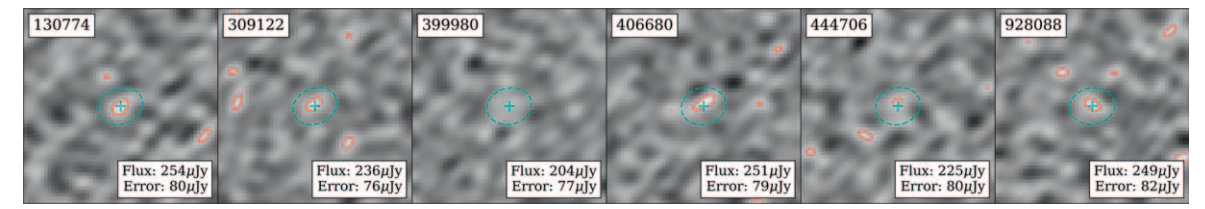


Figure 7. ALMA 1.1 mm images for the six of our 36 quiescent candidates for which $>1\sigma$ ALMA flux was detected, and, based on the estimated obscured SFR, were removed from our quiescent sample; we note that all of these sources in fact have an S/N >2.5 in the ALMA Band 6. The red lines are 3σ contours, the source R.A. and decl. are denoted by the cyan cross, and the fitted ALMA beam is shown as the cyan ellipse. Each stamp is $10'' \times 10''$.

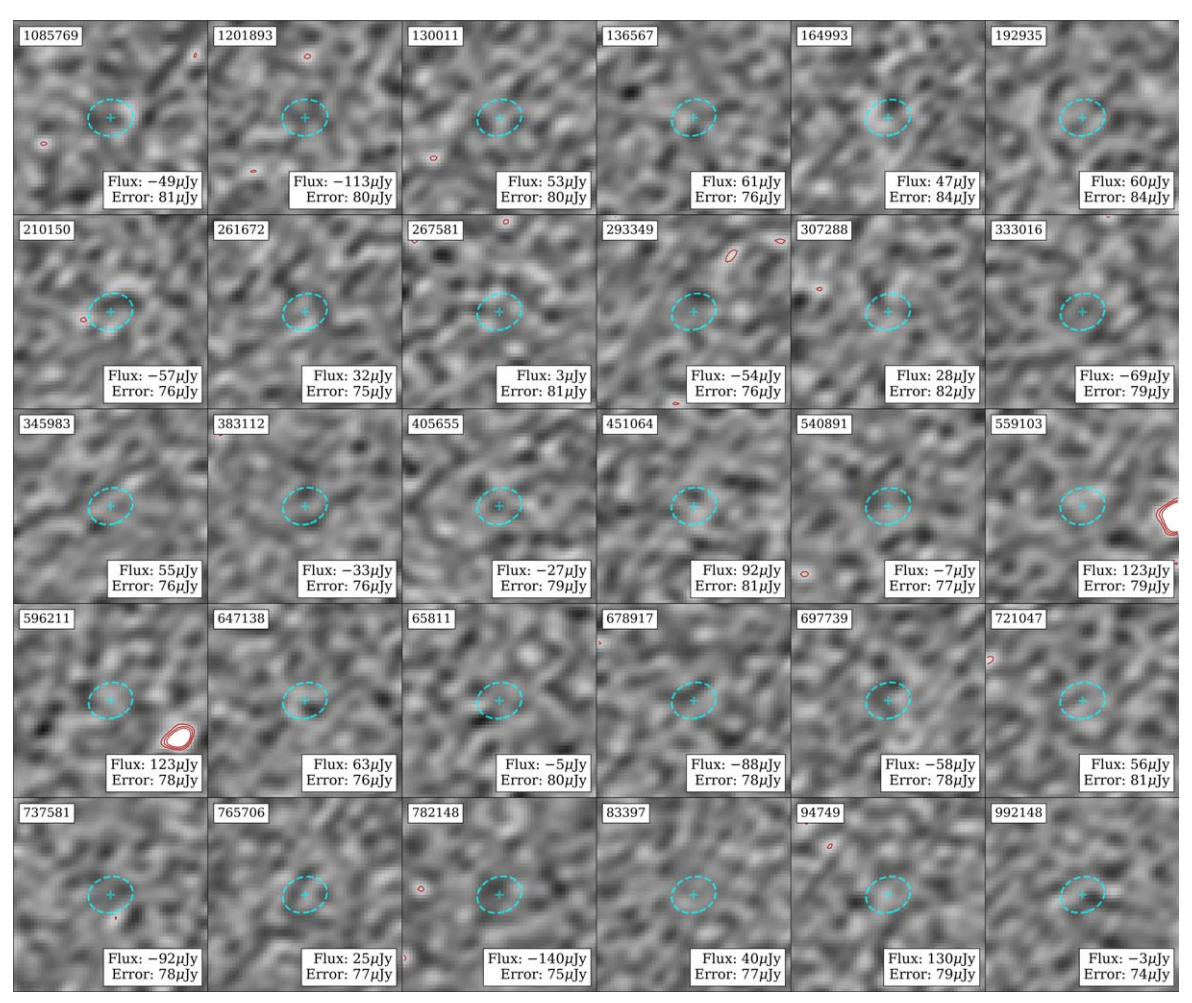


Figure 8. ALMA images for the 30 selected quiescent galaxies. The red lines are 3σ , 4σ , and 5σ contours, the ALMA beam is shown as the cyan ellipse, and the source R.A. and decl. is denoted by the cyan cross. To be characterized as quiescent, we calculate the dust-obscured SFR from the measured flux and require the 1σ upper limit of the SFR to fall 2σ below the SFMS at the galaxy's best-fitting stellar mass. Each stamp is $10'' \times 10''$.

5. Obscured Star Formation Rates and Contamination

ALMA 1.1 mm observations measure dust emission corresponding to dust-obscured star formation, allowing us to remove obvious contaminants from our quiescent sample. In order to determine the obscured SFR of each source, we generate model dust SEDs at our ALMA sensitivity limit based on the prescription of Drew & Casey (2022): we adopt a range of dust temperatures and fit the ALMA 1.1 mm flux to a modified optically thin blackbody with a mid-IR power law of index $\alpha \sim 2$. We take three sample SEDs at the wavelength of the peak dust temperature (T) and the upper and lower T0 range, based on our ALMA sensitivity. For the quiescent

candidates, this corresponds to $T=25\pm5$ K. We then scale each dust SED to the ALMA observations to calculate each galaxy's IR luminosity ($L_{\rm IR}$) by integrating each scaled dust SED from 8–1000 μ m and assuming each source is at the best-fit redshift (also the peak of P(z), z_a) from eazy. From this $L_{\rm IR}$, we then approximate the level of obscured star formation following Kennicutt & Evans (2012), which assumes the Kroupa & Weidner (2003) initial mass function with a Salpeter slope of $\alpha_*=-2.35$ from 1–100 M_\odot and $\alpha_*=-13$ from $0.1-1 M_\odot$:

$$SFR = \log(L_{IR}) - 43.41,$$
 (1)

where SFR is given in M_{\odot} yr⁻¹ and $L_{\rm IR}$ is in erg s⁻¹.

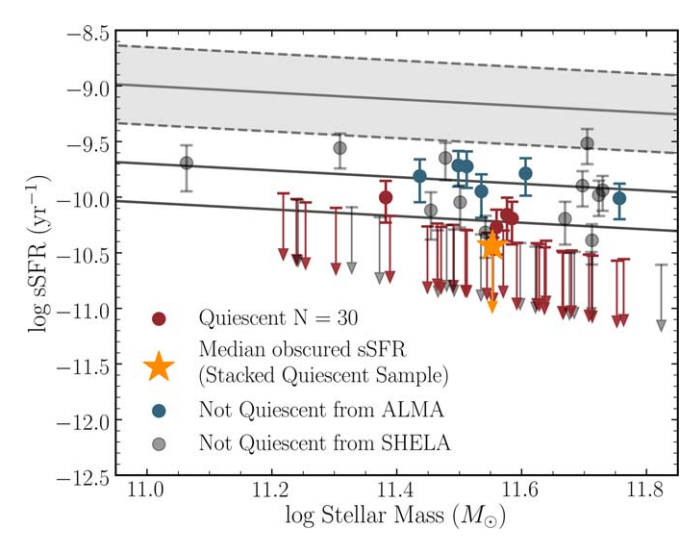


Figure 9. Similar to Figure 3, but shown here are the measured sSFRs based on the ALMA 1.1 mm imaging. The gray shaded region is the 1σ range of the Salmon et al. (2015) SFMS, and the gray solid lines are 2σ and 3σ below the SFMS. The distribution of our 61 high-redshift sources are shown with respect to the SFMS. The gray points are sources removed from our quiescent sample from SED fitting with BAGPIPES (Section 3.2). For the 36/61 sources classified as quiescent from optical data (colored points), we then examine ALMA band 6 1.1 mm observations. Similar to the measured optical SFRs, to be classified as quiescent, we require the 1σ upper limit of the FIR SFR to fall below 2σ of the SFMS for the given best-fit stellar mass as recovered by BAGPIPES. This removed 6/36 sources (shown in blue) from our final quiescent sample (red; see details in Section 5).

To determine $L_{\rm IR}$, each of the 36 sources is fit with a 20, 25, and 30 K (characteristic dust temperature $T=25\pm5\,\rm K$) modified blackbody as described above. For these dust temperatures, a 1σ detection ALMA 1.1 mm flux at our sensitivity limit (\sim 80 μ Jy) would result in an obscured SFR upper limit of \sim 15, 21, and 27 M_{\odot} yr⁻¹, respectively.

Six sources that satisfy our massive quiescent selection have measured dust-obscured SFRs that place them above our sSFR selection threshold using these characteristic dust temperatures. We thus refit these sources using dust models more typical of DSFGs at $z\sim4$, with $T=40\pm5$ K (Sommovigo et al. 2022) and recalculate the dust-obscured SFRs. The ALMA Band 6 images of these sources are shown in Figure 7, and the ALMA fluxes as well as estimated obscured SFRs for these sources are reported in Table 2. We note that the detections by ALMA do not necessarily imply that these are not high-redshift sources, instead it only speaks to the existence of significant star formation activity, and therefore are no longer characterized as quiescent in this conservative sample.

5.1. Quiescent Sample

The removal of the six sources with significant obscured SFRs from our quiescent sample leaves us with a final sample of 30 candidate massive quiescent galaxies. Images for these sources are shown in Figure 8, where the reported errors are the 5σ -clipped rms of the images. This implies that we expect a contamination rate of 6/36, or $\sim 17\%$, based on SED fitting using only SHELA photometry for selecting massive high-redshift quiescent galaxies. To explore the constraints on the obscured SFRs made possible from the ALMA imaging, we create a median stack of the 30 quiescent galaxies, shown in Figure 6. We show the distribution of the measured dust-

obscured star formation with respect to the SFMS of our sample in Figure 9. We determine the median flux of our final quiescent sample by repeating the analysis detailed in Section 4.2 using the beam+position-fixed imfit fit on the stacked image, finding a flux density of $9\pm17~\mu\mathrm{Jy}$, a $<1\sigma$ detection.

We thus calculate the corresponding obscured SFR at the median redshift of our sample in the same way as above, using the 1σ flux error of 17 μ Jy as the flux, and find an obscured SFR upper limit of $<4~M_{\odot}/{\rm yr}^{-1}$. At the median mass of our sample of $\log(M/M_{\odot})=11.5$, this corresponds to an sSFR of $-10.9~{\rm yr}^{-1}$. We show the median stellar mass and upper limit in obscured SFRs of our final sample in Figure 9.

6. Discussion

This work presents a robust exploration into the contamination rate in a sample of z>3 massive quiescent galaxy candidates. The primary contaminants of massive quiescent galaxies at z>3, particularly in the optical–IR range, are lower-redshift ($z\sim1-2$) dust-obscured star-forming galaxies. However, these galaxies will be easily distinguishable at longer wavelengths as this dust will be detected in emission with submillimeter/millimeter observatories such as ALMA.

In this work, we develop a methodology to select high-redshift (z>3) massive quiescent galaxies from broadband imaging robustly (in the SHELA field). We show that by examining ALMA observations for our sample of candidate high-redshift quiescent galaxies, only 6/36 sources have significant ALMA flux. This implies a contamination rate of ~17% from dust-obscured star-forming galaxies with SFRs $\gtrsim 20\,M_\odot/\mathrm{yr}^{-1}$ (calculated using a 1σ detection of 80 μ Jy, corresponding to a log(sSFR/yr⁻¹) < -10.2 at log(M_*/M_\odot) = 11.5). This relatively low contamination rate indicates that future work in the SHELA field using these selection criteria can compose a robust sample of massive quiescent galaxies with limited contamination from DSFGs. This lays the groundwork to leverage the extraordinary volume made available by SHELA to measure robust number densities of these sources across z=3-5.

7. Summary and Future Work

We present a robust selection of high-redshift massive quiescent galaxies based on photometric fitting, with the goal of exploring contamination via ALMA Band 6 1.1 mm imaging. We begin with a parent sample of 100 sources in the SHELA catalog, fit their photometric redshifts using eazy, and limit ourselves to a sample of 61 high-redshift sources using a conservative photometric-redshift selection criteria of 70% of the redshift probability integral P(z) > 2.5.

From these sources, we perform SED fitting using BAGPIPES to constrain the physical properties of each source, and select likely quiescent sources. We found that 36/61 high-redshift sources were quiescent (with SFR $>2\sigma$ below the SFMS from Salmon et al. 2015 at z=4). We then examine ALMA Band 6 1.1 mm imaging, which allows us to rule out significant dust-obscured star formation activity and found 6/36 sources were likely star forming. We determined the obscured SFR by fitting model dust SEDs at our ALMA sensitivity limit based on the prescription of Drew & Casey (2022) to obtain $L_{\rm IR}$. We then approximate the level of obscured star formation following Kennicutt & Evans (2012).

We report the sSFRs of these six sources, confirming that they lie above our quiescent threshold, and removed them from our final sample of massive quiescent galaxies. These results imply that the selection of massive quiescent sources based on SED fitting of the SHELA catalog will have an expected contamination rate of $\sim 17\%$ by DSFGs.

This results in a final sample of 30 massive ($\log(M/M_{\odot}) > 11$) quiescent galaxies at z > 3. It is important to note that this is a preliminary sample, as the goal of this paper is to determine selection criteria and measure the contamination by DSFGs by utilizing ALMA observations. We intend to repeat this SED-fitting process with the updated SHELA catalog (Leung et al. 2023), which will be 1–1.3 mag deeper across all bands, as well as include newly acquired Y-band imaging to constrain our future sample better.

This sample of 30 massive high-redshift quiescent galaxies also provides excellent potential targets for follow-up spectroscopy with JWST NIRSpec. Deep spectroscopy from JWST will be able to detect Balmer absorption features at these redshifts and provide the all-important redshift confirmation for these extreme sources. With NIRSpec, observations of key star formation features (H α emission, Balmer absorption, D_n4000, UV/IR slopes) will also allow investigations into the details of the formation and

subsequent quenching of high-redshift massive quiescent galaxies, which are encoded in their stellar populations.

Acknowledgments

K.C., S.L.F., and G.C.K.L. acknowledge support from the National Science Foundation (NSF) through grant AST-2009905. This material is based upon work supported by the National Science Foundation Graduate Research Fellowship under grant No. DGE 2137420. This paper makes use of the following ALMA data: ADS/JAO.ALMA#2019.1.01219.S. ALMA is a partnership of ESO (representing its member states), NSF (USA), and NINS (Japan), together with NRC (Canada), MOST, and ASIAA (Taiwan), and KASI (Republic of Korea), in cooperation with the Republic of Chile. The Joint ALMA Observatory is operated by ESO, AUI/NRAO, and NAOJ. The National Radio Astronomy Observatory is a facility of the National Science Foundation operated under cooperative agreement by Associated Universities, Inc. A.Y. is supported by an appointment to the NASA Postdoctoral Program (NPP) at NASA Goddard Space Flight Center, administered by Oak Ridge Associated Universities under contract with NASA. We thank Adam Carnall for helpful conversations about the running of Bagpipes.

Appendix A BAGPIPES Fits

The BAGPIPES (optical-IR) SED fits for candidate high-redshift massive quiescent galaxies are shown in Figures 10 and 11. Figure 10 shows the sources that were not detected in ALMA 1.1 mm observations, therefore confirmed to be

quiescent. Figure 11 show sources that have ALMA detections, implying the presence of significant dust-obscured star-formation (Section 5), thus were removed from our final sample of massive quiescent galaxies.

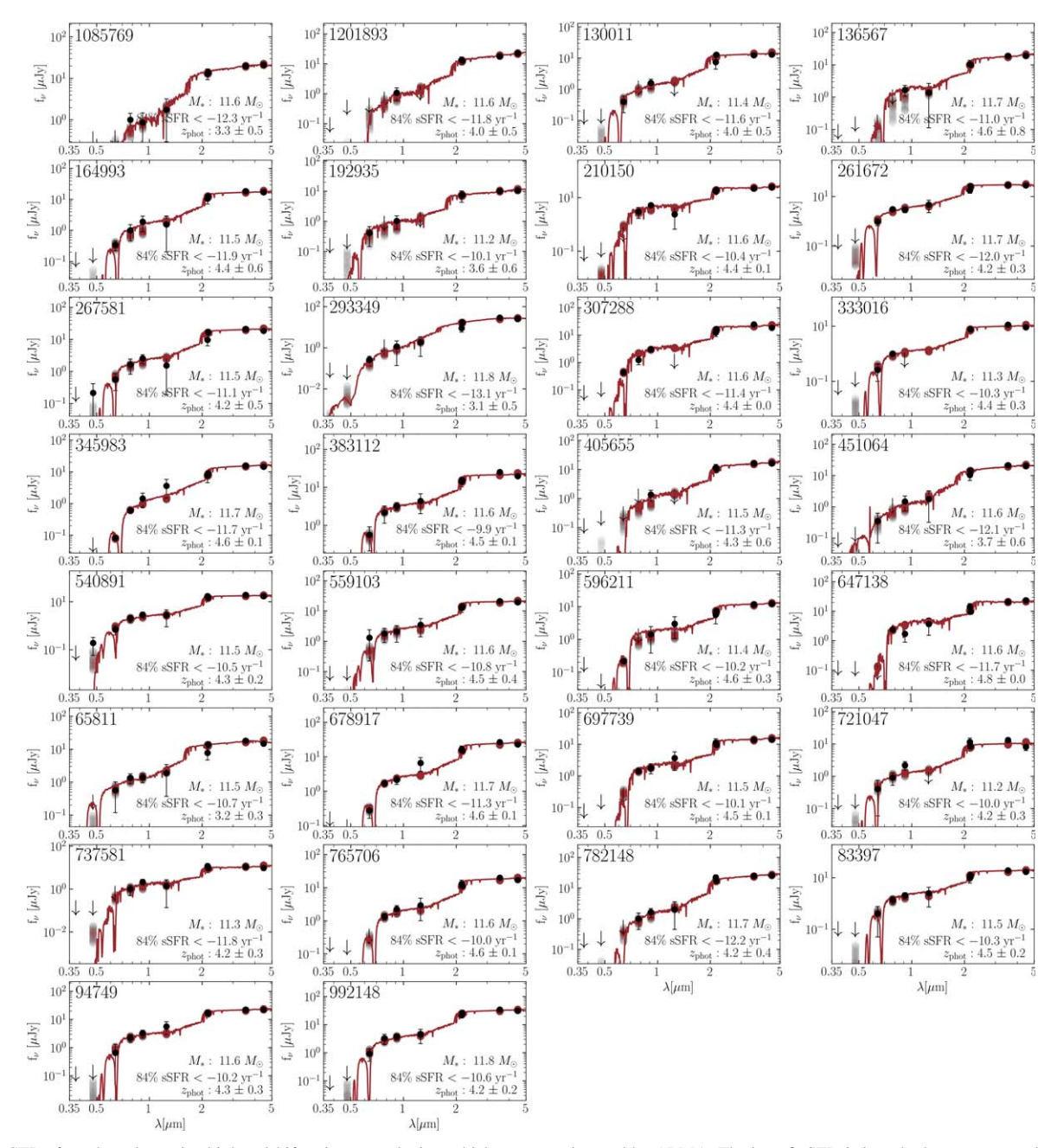


Figure 10. SEDs for selected massive high-redshift quiescent galaxies, which were not detected by ALMA. The best-fit SED is in red, photometry are denoted by the black points, and the red shaded points are 1σ posteriors on the photometry.

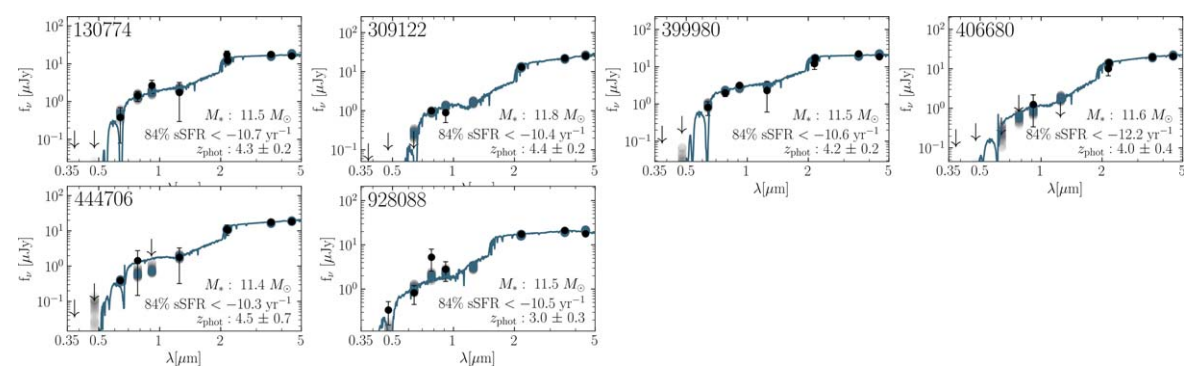


Figure 11. SEDs for candidate massive high-redshift quiescent galaxies, which were removed based on ALMA 1.1 mm flux measurements. While in the optical–IR these sources seem quiescent based on the best-fitting SED, the measured dust-obscured SFR from 1.1 mm flux for these sources place them at $<2\sigma$ below the SFMS at $z \sim 4$. The best-fit SED is in blue, photometry are denoted by the black points, and the blue shaded points are 1σ posteriors on the photometry.

Appendix B ALMA Observations

Here we present ALMA observations for the 62 sources which did not satisfy our selection criteria to be considered high redshift and quiescent. 52 of these sources had no

significant detection in ALMA 1.1 mm imaging, as shown in Figure 13. While the other 10 sources were determined to have a $>3\sigma$ detection in 1.1 μ m, these are shown in Figure 12.

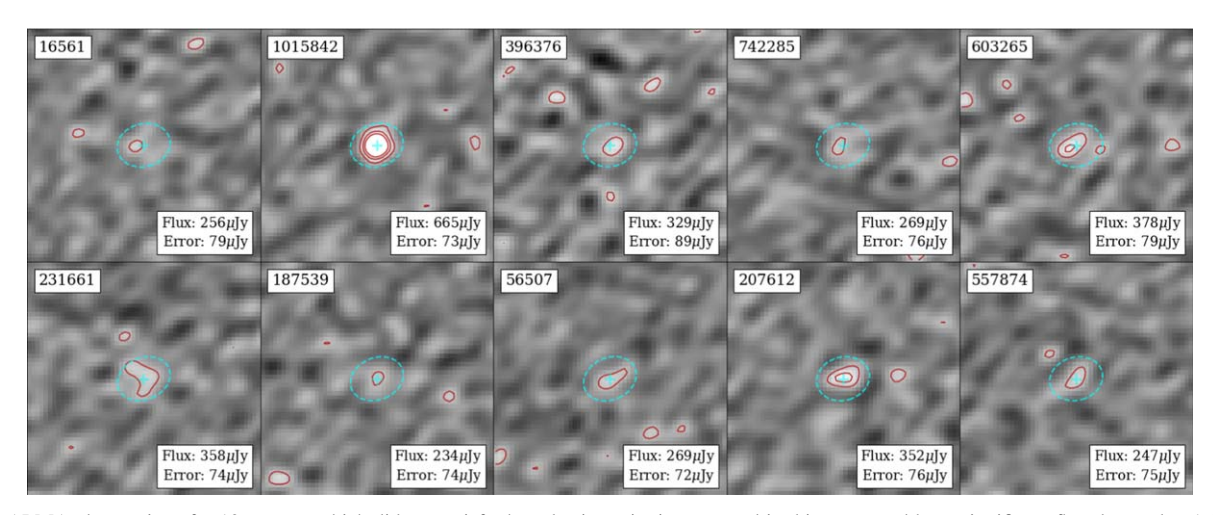


Figure 12. ALMA observations for 10 sources which did not satisfy the selection criteria presented in this paper and have significant flux detected at 1.1 mm. Each stamp is $10'' \times 10''$. These observations indicate the presence of dust-obscured star formation. Some sources have an apparent offset between the source position, indicated by the cyan cross in the center of each stamp, and the ALMA flux. This offset between stellar emission and dust radiation has been observed in several other similar studies (e.g., Maiolino et al. 2015; Franco et al. 2018; Fujimoto et al. 2020), and the ALMA flux detection here has been determined to be from the targeted source and within the K-band PSF.

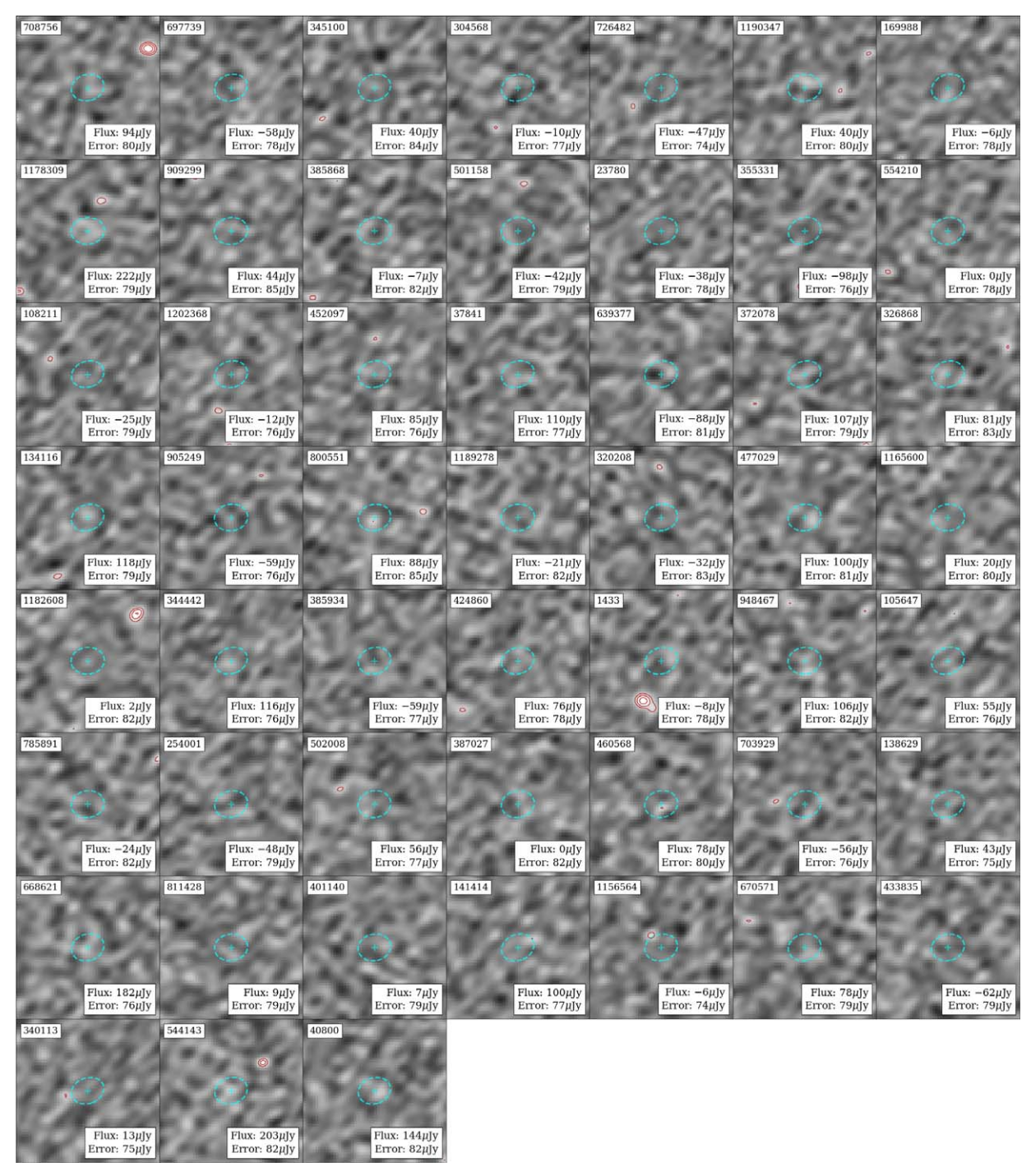


Figure 13. ALMA observations for 52 sources which were not considered high redshift and quiescent. Each stamp is $10'' \times 10''$. These sources do not have significant flux at 1.1 mm. We stress that while we do not include these sources in our final sample, due to the conservative nature of our selection discussed in Section 3, many of these sources do still have sSFRs well below the SFMS.

ORCID iDs

```
Katherine Chworowsky https://orcid.org/0000-0003-
4922-0613
Steven L. Finkelstein https://orcid.org/0000-0001-
8519-1130
Justin S. Spilker https://orcid.org/0000-0003-3256-5615
Gene C. K. Leung https://orcid.org/0000-0002-9393-6507
Micaela B. Bagley https://orcid.org/0000-0002-9921-9218
Caitlin M. Casey https://orcid.org/0000-0002-0930-6466
Caryl Gronwall https://orcid.org/0000-0001-6842-2371
Shardha Jogee https://orcid.org/0000-0002-1590-0568
Rebecca L. Larson https://orcid.org/0000-0003-2366-8858
Casey Papovich https://orcid.org/0000-0001-7503-8482
Rachel S. Somerville https://orcid.org/0000-0002-6748-6821
Matthew Stevans  https://orcid.org/0000-0001-8379-7606
Isak G. B. Wold https://orcid.org/0000-0002-0784-1852
L. Y. Aaron Yung https://orcid.org/0000-0003-3466-035X
```

References

```
Baldry, I. K., Glazebrook, K., Brinkmann, J., et al. 2004, ApJ, 600, 681
Balogh, M. L., Baldry, I. K., Nichol, R., et al. 2004, ApJL, 615, L101
Barbary, K. 2016, JOSS, 1, 58
Bell, E. F., Wolf, C., Meisenheimer, K., et al. 2004, ApJ, 608, 752
Brammer, G. B., van Dokkum, P. G., & Coppi, P. 2008, ApJ, 686, 1503
Brammer, G. B., Whitaker, K. E., van Dokkum, P. G., et al. 2011, ApJ, 739, 24
Brennan, R., Pandya, V., Somerville, R. S., et al. 2015, MNRAS, 451, 2933 Capak, P. L., Carilli, C., Jones, G., et al. 2015, Natur, 522, 455
Carnall, A. C., McLeod, D. J., McLure, R. J., et al. 2023, MNRAS, 522, 3138
Carnall, A. C., McLure, R. J., Dunlop, J. S., & Davé, R. 2018, MNRAS,
   480, 4379
Casey, C. M., Hodge, J., Zavala, J. A., et al. 2018, ApJ, 862, 78
Cecchi, R., Bolzonella, M., Cimatti, A., & Girelli, G. 2019, ApJL, 880, L14
Choi, K., Rott, C., & Itow, Y. 2014, JCAP, 2014, 049
Conroy, C., & Gunn, J. E. 2010, ApJ, 712, 833
Conroy, C., Gunn, J. E., & White, M. 2009, ApJ, 699, 486
Davé, R., Anglés-Alcázar, D., Narayanan, D., et al. 2019, MNRAS, 486, 2827
De Lucia, G., & Blaizot, J. 2007, MNRAS, 375, 2
Dickey, C. M., Starkenburg, T. K., Geha, M., et al. 2021, ApJ, 915, 53
Drew, P. M., & Casey, C. M. 2022, ApJ, 930, 142
Faber, S. M., Willmer, C. N. A., Wolf, C., et al. 2007, ApJ, 665, 265
Fabian, A. 2012, ARA&A, 50, 455
Fang, G., Kong, X., Chen, Y., & Lin, X. 2012, ApJ, 751, 109
Forrest, B., Annunziatella, M., Wilson, G., et al. 2020, ApJL, 890, L1
Franco, M., Elbaz, D., Béthermin, M., et al. 2018, A&A, 620, A152
Fraser-McKelvie, A., & Cortese, L. 2022, ApJ, 937, 117
```

```
Fujimoto, S., Ouchi, M., Shibuya, T., & Nagai, H. 2017, ApJ, 850, 83
Fujimoto, S., Silverman, J. D., Bethermin, M., et al. 2020, ApJ, 900, 1
Gebhardt, K., Cooper, E. M., Ciardullo, R., et al. 2021, ApJ, 923, 217
Glazebrook, K., Schreiber, C., Labbé, I., et al. 2017, Natur, 544, 71
Hill, G. J., Gebhardt, K., Komatsu, E., et al. 2008, in ASP Conf. Ser. 399,
  Panoramic Views of Galaxy Formation and Evolution, ed. T. Kodama,
   T. Yomada, & K. Aoki (San Francisco, CA: ASP), 115
Ikarashi, S., Caputi, K. I., Ohta, K., et al. 2017, ApJL, 849, L36
Kennicutt, R. C., & Evans, N. J. 2012, ARA&A, 50, 531
King, A., & Pounds, K. 2015, ARA&A, 53, 115
Kriek, M., & Conroy, C. 2013, ApJL, 775, L16
Kriek, M., van Dokkum, P. G., Franx, M., et al. 2006, ApJL, 649, L71
Kroupa, P., & Weidner, C. 2003, ApJ, 598, 1076
Lang, D., Hogg, D. W., & Mykytyn, D. 2016, The Tractor: Probabilistic
   Astronomical Source Detection and Measurement, Astrophysics Source
  Code Library, ascl:1604.008
Leung, G. C. K., Finkelstein, S., Weaver, J., et al. 2023, arXiv:2301.00908
Maiolino, R., Carniani, S., Fontana, A., et al. 2015, MNRAS, 452, 54
Marchesini, D., & van Dokkum, P. G. 2007, ApJ, 663, L89
Marrese, P., Marinoni, S., Fabrizio, M., & Altavilla, G. 2018, A&A, 621
Merlin, E., Fontana, A., Castellano, M., et al. 2018, MNRAS, 473, 2098
Merlin, E., Fortuni, F., Torelli, M., et al. 2019, MNRAS, 490, 3309
Muzzin, A., Marchesini, D., Stefanon, M., et al. 2013, ApJ, 777, 18
Newman, A. B., Belli, S., Ellis, R. S., & Patel, S. G. 2018, ApJ, 862, 125
Oke, J. B., & Gunn, J. E. 1983, ApJ, 266, 713
Papovich, C., Shipley, H. V., Mehrtens, N., et al. 2016, ApJS, 224, 28
Rinaldi, P., Caputi, K. I., van Mierlo, S. E., et al. 2022, ApJ, 930, 128
Salim, S., Boquien, M., & Lee, J. C. 2018, ApJ, 859, 11
Salmon, B., Papovich, C., Finkelstein, S. L., et al. 2015, ApJ, 799, 183
Sandles, L., Curtis-Lake, E., Charlot, S., Chevallard, J., & Maiolino, R. 2022,
            515, 2951
Santini, P., Merlin, E., Fontana, A., et al. 2019, MNRAS, 486, 560
Schreiber, C., Glazebrook, K., Nanayakkara, T., et al. 2018, A&A,
Schreiber, C., Pannella, M., Leiton, R., et al. 2017, A&A, 599, A134
Scoville, N., Sheth, K., Aussel, H., et al. 2016, ApJ, 820, 83
Somerville, R. S., & Davé, R. 2015, ARA&A, 53, 51
Sommovigo, L., Ferrara, A., Carniani, S., et al. 2022, MNRAS, 517, 5930
Speagle, J. S., Steinhardt, C. L., Capak, P. L., & Silverman, J. D. 2014, ApJS,
  214, 15
Spitler, L. R., Straatman, C. M. S., Labbé, I., et al. 2014, ApJL, 787, L36
Springel, V., White, S. D. M., Jenkins, A., et al. 2005, Natur, 435, 629
Stefanon, M., Marchesini, D., Muzzin, A., et al. 2015, ApJ, 803, 11
Stefanon, M., Rudnick, G. H., Marchesini, D., Brammer, G. B., &
  Whitaker, K. E. 2013, ApJ, 768, 14
Stevans, M. L., Finkelstein, S. L., Kawinwanichakij, L., et al. 2021, ApJ,
Straatman, C. M. S., Labbé, I., Spitler, L. R., et al. 2015, ApJL, 808, L29
Valentino, F., Tanaka, M., Davidzon, I., et al. 2020, ApJ, 889, 93
Viero, M. P., Asboth, V., Roseboom, I. G., et al. 2014, ApJS, 210, 22
Wold, I. G. B., Kawinwanichakij, L., Stevans, M. L., et al. 2019, ApJS, 240, 5
```